Atmospheric
Measurement
Techniques

Multi-star calibration in starphotometry

Liviu Ivănescu and Norman T. O'Neill

Département de géomatique appliquée, Université de Sherbrooke, Sherbrooke, QC, Canada

Correspondence: Liviu Ivănescu (liviu.ivanescu@usherbrooke.ca)

Abstract. We explored the improvement in starphotometry accuracy using a multi-star Langley calibration in lieu of the more traditional one-star Langley approach. Our goal was a 0.01 calibration-constant repeatability accuracy, at an operational sea-level facility such as our Arctic site at Eureka. Multi-star calibration errors were systematically smaller than single-star errors and, in the mid-spectrum, approached the 0.01 target for an observing period of 2.5 h. Filtering out coarse-mode (supermicrometre) contributions appears mandatory for improvements. Spectral vignetting, likely linked to significant UV/blue spectrum errors at large air mass, may be due to a limiting field of view and/or sub-optimal telescope collimation. Starphotometer measurements acquired by instruments that have been designed to overcome such effects may improve future star magnitude catalogues and consequently starphotometry accuracy.

1 Introduction

Starphotometry involves the measurement of attenuated starlight in semi-transparent atmospheres as a means of extracting the spectral optical depth and thereby estimating columnar properties of absorbing and scattering constituents such as aerosols, trace gases and optically thin clouds. Dedicated instrument development already began in the late 1950s (Dachs, 1960, 1966; Dachs et al., 1966), with increased activity after 2000 (Théorêt, 2003; Gröschke et al., 2009; Pérez Ramírez, 2010; Oh, 2015). One of the earliest comprehensive investigations of starphotometry errors and their influence on calibration was reported in the astronomical literature by Young (1974). Calibration strategies for retrieving accurate photometric observations in variable optical depth conditions were proposed by Rufener (1964, 1986). Those studies were recently updated and complemented using measure-

ments from our High Arctic, sea-level observatory at Eureka, NU, Canada (Ivănescu, 2015; Baibakov et al., 2015; Ivănescu et al., 2021), using a commercial-spectrometer-based starphotometer[1], attached to a Celestron C11 telescope. This, more recent, work underscored certain challenges in performing calibration at such a high-latitude/low-altitude site. The remoteness of the Eureka site and the significant infrastructure requirements of the starphotometer render calibration campaigns at a dedicated mountain site, onerous. The alternative to a calibration campaign (particularly at an Arctic site like Eureka) is to improve on-site calibration methods by overcoming the relatively large optical depth variability typical of operational sites. Much can be learned by exploring this option at an Arctic location like Eureka (see O'Neill et al., 2016, for a discussion of optical depth variability).

Star-dependent (one-star) Langley calibration that depends on large air mass variations is the current standard in starphotometry (see Pérez-Ramírez et al., 2008, 2011). This is mainly due to the limited accuracy of available extraterrestrial star magnitudes (Ivănescu et al., 2021). A good number of High Arctic stars cannot, however, be calibrated in such a way since they do not go through large elevation (i.e. air mass) changes (in the extreme case of a site at the pole, there are no elevation changes). Our goal is to demonstrate that a sub-0.01 optical depth error (partly linked to calibration errors) can be achieved by performing the type of instrument-dependent, star-independent calibration referred to in Ivănescu et al. (2021).

---

[1]Made by Dr. Schulz & Partner GmbH (currently closed).

2   Calibration methodology

2.1   Langley calibration

The starphotometer retrieval algorithm is based on extraterrestrial and atmospherically attenuated magnitudes of non-variable bright stars, denoted by M_0 (provided by the Pulkovo catalogue of Alekseeva et al., 1996) and M, respectively (see Ivănescu et al., 2021, for a more comprehensive elaboration of this section). Their corresponding instrument signals, expressed in terms of magnitude, are $S_0 = -2.5\log F_0$ and $S = -2.5\log F$, respectively, with F_0 and F being the actual measurements in counts s^{-1}. The star-independent conversion factor between the catalogue and instrument magnitudes is (Ivănescu et al., 2021)

$$C = M - S \tag{1}$$
$$C = M_0 - S_0. \tag{2}$$

The C factor accounts for the optical and electronic throughput of the starphotometer, as well as the photometric system transformation between the instrument signal magnitude and the extraterrestrial catalogue magnitude. In terms of magnitude, the Beer–Bouguer–Lambert atmospheric attenuation law is

$$M = M_0 + (m/0.921)\tau, \tag{3}$$

where m is the observed air mass, and τ is the total optical depth. Inserting Eq. (1) yields

$$M_0 - S = -\tau x + C, \tag{4}$$

where $x = m/0.921$. This expression can be used to retrieve C from a linear regression of $M_0 - S$ versus x, if τ is assumed constant. Such a procedure is referred to as the Langley calibration technique or Langley plot. In the absence of an accurate M_0 spectrum, Eq. (2) can be used to transform Eq. (4) into

$$S = \tau x + S_0 \tag{5}$$

for which a catalogue is no longer required. This linear regression enables the retrieval of S_0 instead of C and thus represents a star-dependent calibration.

The right side of Eq. (4) notably indicates that $M_0 - S$ is star independent: it thus represents a linear regression that any star can contribute to and, accordingly, a framework for multi-star Langley calibration.

3   Calibration errors

3.1   Measurement accuracy

The differential of (rearranged) Eq. (4) yields the calibration accuracy error:

$$\delta_C = (\delta_x \tau + x\delta_\tau) - \delta_S + \delta_{M_0}. \tag{6}$$

The $(\delta_x \tau + x\delta_\tau)$ component underscores the rationale for performing calibrations at a high-altitude site (where τ, δ_τ and $\delta_x \tau$ are typically smaller) and the advantage of maintaining small x in order to minimize the $x\delta_\tau$ contribution to δ_C. The sky stability during the retrieval of C may be monitored by computing τ for each sample, with Eq. (4). The δ_S error component accounts for any systematic signal changes: optical transmission degradation, misalignment error and star spot vignetting, etc. The δ_{M_0} component accounts for any magnitude bias in the bright-star catalogue (i.e. the average of accuracy-error spectra for all catalogue stars: see Ivănescu et al., 2021, for a detailed discussion of error bias in the Pulkovo and other catalogues). Because it is a catalogue-specific constant, the optical depth retrieval accuracy will not be affected by its consistent use[2].

3.2   Regression precision

A linear regression applied to a plot of $y = M_0 - S$ versus x yields the slope $(-\hat{\tau})$ and intercept $(\hat{C})$ of the Langley Eq. (4). The regression equation is then $\hat{y} = -\hat{\tau}x + \hat{C}$, and the linear-fit residuals are represented by $r = y - \hat{y}$. The standard error of the regression slope and intercept for a large number of measurements[3] can be expressed as (see, for example, Montgomery and Runger, 2011)

$$\sigma_{\hat{\tau}} = \frac{\sigma_{\bar{r}}}{\sigma_x}, \qquad \sigma_{\hat{C}} = \sigma_{\hat{\tau}}\sqrt{\overline{x^2}}. \tag{7}$$

It should be noted that $\bar{r}$ (the mean of the residual) $= 0$ is a corollary of the linear regression constraints.

The Langley calibration y axis embodies two independent sets of measurements: N "measurements" of M_0 and n measurements of S. From a pure-noise standpoint, the residuals can be represented by an ensemble of individual measurements $(r = (M_0 - S) - (-\tau x + C))$ where each parameter (except C) is subject to noisy variation. Excluding the typically negligible random errors in x yields[4]

$$\sigma_{\bar{r}}^2 = \frac{\sigma_{\epsilon_S}^2}{n} + \frac{\sigma_{\epsilon_\tau}^2 \overline{x^2}}{n} + \frac{\sigma_{\epsilon_{M_0}}^2}{N} = \sigma_{\bar{\epsilon}_S}^2 + \sigma_{\bar{\epsilon}_\tau}^2 \overline{x^2} + \sigma_{\bar{\epsilon}_{M_0}}^2, \tag{8}$$

where the standard error expression for a linear combination of random variables was employed (Barford, 1985). The subscript ϵ represents a single instance of a random (noise) mea-

---

[2]Such an error becomes part of the C value extracted from the Langley calibration of Eq. (4) and becomes part of the operational retrieval process when Eq. (4) is inverted to yield individual values of τ.

[3]$n > 10$, where $n = \sum n_i$ (n_i being the number of observations associated with star i).

[4]Where $\epsilon_\tau x = \epsilon_\tau x + \tau \epsilon_x = \epsilon_\tau x$ (since $\epsilon_x = 0$) and the variance of the $\epsilon_\tau x$ product (Goodman, 1960) is $\sigma_{\epsilon_\tau x}^2 = \sigma_x^2 \overline{\epsilon_\tau}^2 + (\sigma_{\epsilon_\tau}^2 \overline{x}^2 + \sigma_{\epsilon_\tau}^2 \sigma_x^2) = \sigma_x^2 \overline{\epsilon_\tau}^2 + \sigma_{\epsilon_\tau}^2 \overline{x^2} = \sigma_\tau^2 \overline{x^2}$, since $\overline{\epsilon}_\tau = 0$, $\sigma_{\epsilon_\tau} = \sigma_\tau$ and $\sigma_x^2 = \overline{x^2} - \overline{x}^2$.

surement in S, τ or M_0, and σ_ϵ is its zero-mean standard deviation. σ_{ϵ_τ} was replaced by σ_τ because no systematic variation was assumed in τ during the calibration period. ϵ_{M_0} represents the difference between an individual star's M_0 accuracy errors and the averaged M_0 catalogue bias. The $\sigma_{\epsilon_{M_0}}$ term is specific for the use of multiple stars during the calibration.

4 Observing conditions

The assumption of constant τ in time (t) and observational direction (expressed in terms of m) may be problematic over long observation periods and large air mass changes. It is a useful exercise to assess the average time period and air mass range over which a degree of τ constancy (sky stability) is maintained.

Variations of a sky instability parameter ($\sigma_{\delta\tau}$) were analyzed using $\delta\tau$ differences for τ measurements acquired during the 2019–2020 season in Eureka. $\delta\tau$ values were placed into (a) fixed Δt bins to generate $\delta\tau$ histograms for high stars (where $\delta\tau = \tau_f - \tau_i$ is computed from a later time (f) relative to an earlier time (i)) and (b) fixed Δm bins from high- to low-star m pairs. Since δ values of each bin generally come from distinct periods, τ_f and τ_i are expected to be uncorrelated: the τ_i versus τ_f correlation coefficient was determined to be < 0.25 when $\tau_p < 0.1$, $\Delta t < 1$ h and ~ 0.1 otherwise (see the legend of Fig. 1 for the definition of τ_p). This is negligible for the purposes of our analysis, and, accordingly, they can be considered as independent variables. The approximation $\sigma_\tau \cong \sigma_{\delta\tau}/\sqrt{2}$ (Soch et al., 2021) can accordingly be employed for each Δm or Δt bin.

Those histograms often included anisotropic outliers typical of lognormal τ statistics (Sayer and Knobelspiesse, 2019). A median approach was chosen to render the statistics approximately independent of the outliers: the MAD (median absolute deviation) parameter was employed as a robust measure of histogram width (see Eq. 1.3 in Rousseeuw and Croux, 1993, for MAD details). In order to eventually convert the statistics to those of a normal distribution, an outlier cutoff of $4.5 \cdot$ MAD was defined[5]. This particular cutoff is equivalent to the classical normal distribution outlier cutoff of 3σ since $\sigma = 1.5 \cdot$ MAD.

Figure 1 shows σ_τ (computed after the outlier cutoff and using the σ_τ approximation given above) as a function of (a) Δt and (b) Δm. It can be shown[6] that a calibration period of 2 h, for which $n \simeq 46$ at the standard sampling rate of starphotometer, yields $\sigma_\tau \simeq 1.4\sigma_{\hat{C}}$. This means that the cal-

---

[5]A cutoff liberty that we availed ourselves of because one is free to choose the duration of the calibration period and/or to perform outlier filtering prior to Langley regressions.

[6]Using $\sigma_\tau^2 \simeq \sigma_{\hat{C}}^2 n/k_3$ (obtained from Eq. B3), with the terms in S and M_0 neglected, and inserting $\sigma_\tau/\sqrt{n}$ (i.e. $\sigma_{\bar{\tau}}$) into Eq. (7) and noting that a typical range of $x \in [1.086, 5]$ yields $k_3 \simeq 23$ (see Fig. B1).
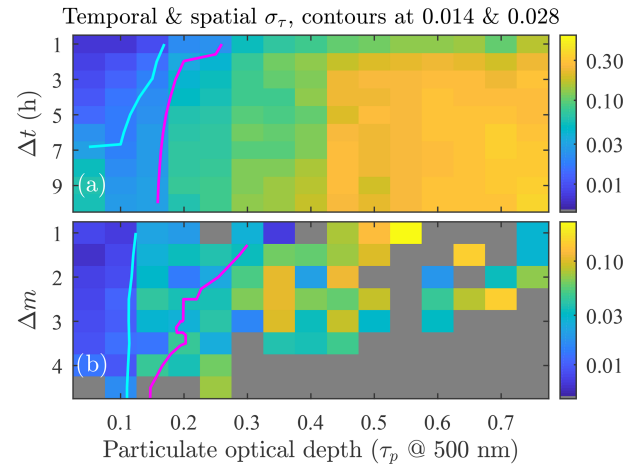

Figure 1. Two-dimensional sky instability (σ_τ) patterns for the 2019–2020 season at Eureka. The colour-coded σ_τ values are computed relative to a reference τ value but plotted as a function of its associated particulate optical depth ($\tau_p = \tau - \tau_m$, where τ_m is the molecular scattering optical depth) and **(a)** time difference (Δt) or **(b)** air mass difference (Δm). The magenta and purple curves represent the column-wise averaged $\sigma_\tau = 0.014$ and 0.028 contour lines. There were many more data associated with Δt than with Δm bins (i.e. more robust bin statistics are expected in the former case). Note that Δm and Δt were chosen to be positive.
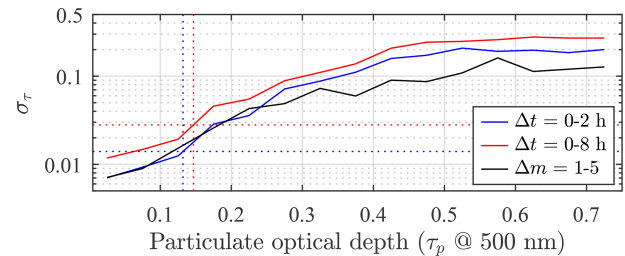
Figure 2. σ_τ vs τ_p for the three calibration scenarios defined.

ibration error ($\sigma_{\hat{C}}$) is limited to < 0.01 only if $\sigma_\tau < 0.014$. An 8 h observing period enables a more generous limit of $\sigma_\tau < 0.028$ to achieve the same calibration precision. Contour curves of $\sigma_\tau = 0.014$ and 0.028 are superimposed on Fig. 1.

Figure 2 shows the σ_τ variability estimation for the 2 h "fast" and the 8 h "long" calibration periods, as well as a third scenario with $\Delta m = 1$ to 5. The three curves represent the standard deviation (after cutoff) of the corresponding range-aggregated data. They tend to converge with decreasing τ_p: the 2 h and 8 h σ_τ values of 0.014 and 0.028 correspond to τ_p values of 0.13 and 0.15, respectively (vertical dashed blue and red lines defined by the intersection with the corresponding horizontal 0.014 and 0.028 lines). The cases $\tau_p \leq 0.13$ and 0.15 were labelled as "clear-sky" conditions because of their tendency to promote calibration stability. Their corresponding clear-sky statistics are presented in Appendix A.
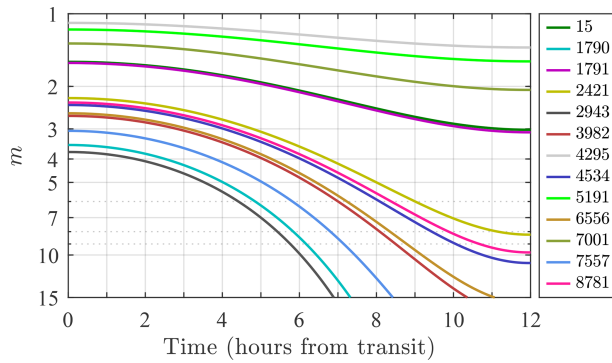
Figure 3. Air mass versus time past the transit for the bright stars observable at Eureka (identified by their HR catalogue index). The transit of a given star occurs when it crosses the local meridian (minimum air mass).
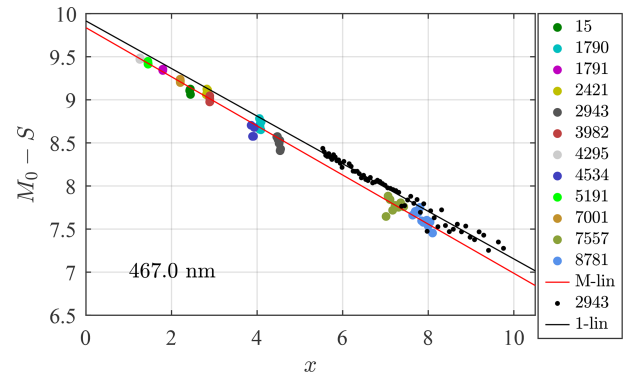

Figure 4. One- and multi-star Langley calibrations (both lasting about 2.5 h; see Appendix A). The one-star and multi-star measurement points are represented, respectively, by small black dots and large solid-coloured circles, while their linear regression fits appear as solid lines (1-lin and M-lin, respectively). Each point represents an average of five 6 s exposures. Each star is identified by their HR IDs (see Table B1 in Ivănescu et al., 2021).

Many High Arctic stars are circumpolar (i.e. they never set), and thus their air mass range is limited. Figure 3 shows air mass variation as a function of time past the transit for our dataset of the 13 brightest (and stable) stars at Eureka.

A well-defined separation is notable between high stars ($m(12\,\mathrm{h}) < 3.1$) and low stars ($m(0\,\mathrm{h}) > 2.2$). A large air mass range is clearly only available for the low stars (i.e. about two-thirds of our Eureka bright-star dataset). However, star vignetting, due to turbulence-inducing star-spot expansion beyond the boundaries of the field of view (FOV), may affect the optical throughput of the Eureka system at $m > 5$ (Ivănescu et al., 2021). This type of air mass constraint, combined with the low-star constraints of Fig. 3, results in only moderate Δm excursions (at the expense of substantial Δt) if only a single star is employed in a Langley-type calibration. A multi-star calibration can be exploited to mitigate such Δm and Δt limitations.

5 Multi-star calibration

This type of calibration exploits a singular advantage of starphotometry over moonphotometry and sunphotometry: the capability of employing multiple extraterrestrial light sources in a relatively short period of time. In comparison with a C-determining Langley calibration using one star, the multi-star approach enables a synergistic Langley calibration that employs several stars exhibiting a wide range of air mass values over a significantly shorter period of time.

One- and multi-star Langley calibrations acquired with the Eureka starphotometer on 7 December 2019 and 10 January 2020, respectively, are shown in Fig. 4. The observations for $x > 5$ were carried out to highlight any vignetting effect due to the aforementioned star-spot expansion. The one-star case (small black dots and their associated "1-lin" regression line) shows the results for the low Procyon star (HR 2943, spectral type F5V). Its colder temperature ensures a near-infrared (NIR) brightness that is larger than all the other bright stars of

Fig. 3[7]. That reason aside, it is also, arguably, the most optimal one-star Langley-regression choice since no other Fig. 3 bright star can duplicate its large and rapid air mass change (see the lowest black curve).
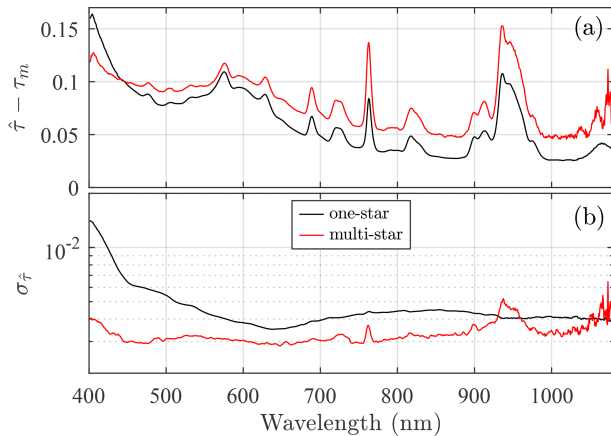
5.1 Calibration precision

The resulting one- and multi-star $\hat{\tau}$ spectra (each spectral point representing a linear-regression Langley slope) are shown in Fig. 5a. Their associated precision errors ($\sigma_{\hat{\tau}}$) of Eq. (7) are shown in Fig. 5b. One should note that the estimated multi-star error is substantially and consistently smaller than that of the one-star calibration. The $\hat{C}$ and $\sigma_{\hat{C}}$ spectra from the Langley regressions are shown in Fig. 6a and b, respectively. The $\sigma_{\hat{C}}$ values are, in the multi-star case, significantly smaller and closer to the 0.01 target.

The generally smaller $\sigma_{\hat{\tau}}$ values of the multi-star case are partly attributable to the one-star case being limited to a relatively smaller x range (i.e. smaller σ_x in Eq. 7), while the smaller $\sigma_{\hat{C}}$ values are partly attributable to the smaller $\sigma_{\hat{\tau}}$ values and the lower values of $\overline{x^2}$ (see Eq. 7). The $\sigma_{\hat{C}}$ increases in the ultraviolet (UV) and NIR are discussed in Sect. 6.2. The peak around 940 nm is likely associated with a faint and noisy star signal induced by strong attenuation in the water vapour absorption band, coupled with the non-linear nature of the optical depth in that spectral region (Pérez-Ramírez et al., 2012).
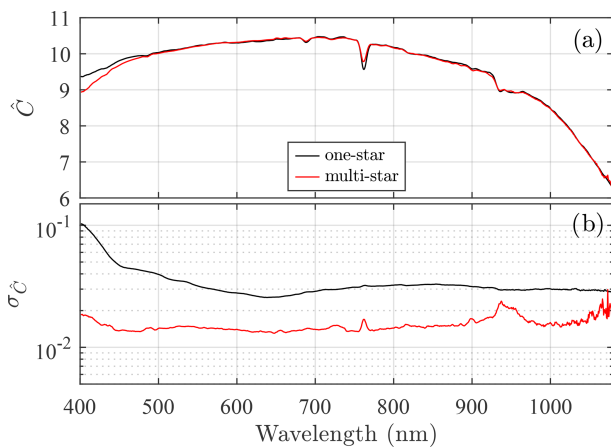
5.2 Repeatability

The robustness of the $\sigma_{\hat{C}}$ spectra of Fig. 6b and the impact of potential systematic errors can be investigated with repeata-

---

[7]The other bright stars, being of similar A–B type (Ivănescu et al., 2021), exhibit lower signal-to-noise ratios (SNRs) in the NIR.
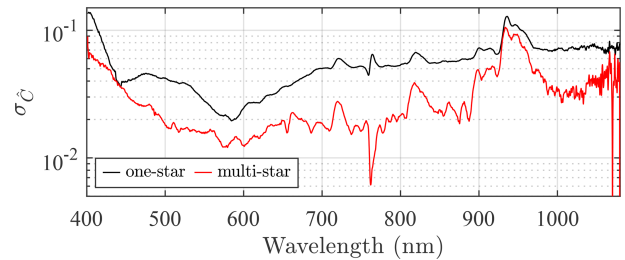
Figure 5. (a) One- and multi-star Langley-regression slopes (expressed as $\hat{\tau}_p = \hat{\tau} - \tau_m$). **(b)** $\sigma_{\hat{\tau}}$ values derived from Eq. (7).

Figure 6. (a) $\hat{C}$ retrieved from the one- and multi-star Langley calibrations. **(b)** $\sigma_{\hat{C}}$ values computed using Eq. (7).

Figure 7. $\sigma_{\hat{C}}$ curves derived for three one-star Langley calibrations acquired using the Procyon (HR 2943) star on 7 December 2019, 5 January 2020 and 16 January 2020, as well as three multi-star calibrations acquired on 10 March 2018, 7 December 2019 and 10 January 2020. These spectra are generally similar to Fig. 6b results.

6 Regression error discussion

6.1 Data processing

Figure 8 shows dual-wavelength (400 and 1000 nm) regression tests for two of the three one-star calibrations of the previous section (two of the three dates given in the legend of Fig. 7 for the HR 2943 star) plus a third hotter star (HR 3982, spectral type B7) that was specifically chosen to better understand the influence of temperature-driven spectral differences in the target star. The smaller regression slope and point dispersion about the HR 3982 regression line, compared with the two HR 2943 cases, are noticeable at both wavelengths (notably at 1000 nm) and are an indicator of generally clearer sky conditions.

The C values retrieved from linear regressions over an increasing x range in Fig. 8 (from the smallest x value to an artificial maximum of x_{max}) are plotted in Fig. 9. The damping out of regression noise and the asymptotic approach to the horizontal pan-x regression value as x_{max} increases can be readily observed in all three plots.

The corresponding slope-derived τ_p spectra are shown in Fig. 10 for three x_{max} cases (the three coloured spectra were derived for x_{max} values corresponding to the matching colours of the three vertical lines in Figs. 8 and 9). The x-dependent regression error dynamics are investigated in Appendix C. The next subsection describes potential competing causes of C variations and makes a link to τ_p errors[9].

6.2 Regression error interpretation

The sky instability plots of Fig. 1 show that the standard deviation of the optical depth increases with time and air mass separation between any two stars (this applies equally well to the variation between two positions of the same star). A systematic optical depth drift during the calibration leads to a

bility experiments. The $\hat{C}$ spectra employed to produce the standard deviations[8] shown in Fig. 7 were derived from three one-star and three multi-star Langley calibrations that were well separated in time (i.e. they were optically independent in terms of any significant correlations between the τ_p variations of each period) and nearly satisfied the clear-sky calibration constraints of Sect. 4. The Fig. 7 error spectra are, with the exception of larger differences in certain spectral regions, roughly coherent with the Fig. 6b spectra (including the fact that the one-star errors are significantly larger than the multi-star errors).

---

[8]Standard deviations that, we would argue, are also standard errors (each of the three $\hat{C}$ spectra that were averaged were more akin to means).

[9]The strong, positive correlation between C and τ_p and between their errors is the result of variations in the regression lines being effectively driven by rotations about a cluster of pivot points whose x position changes little.
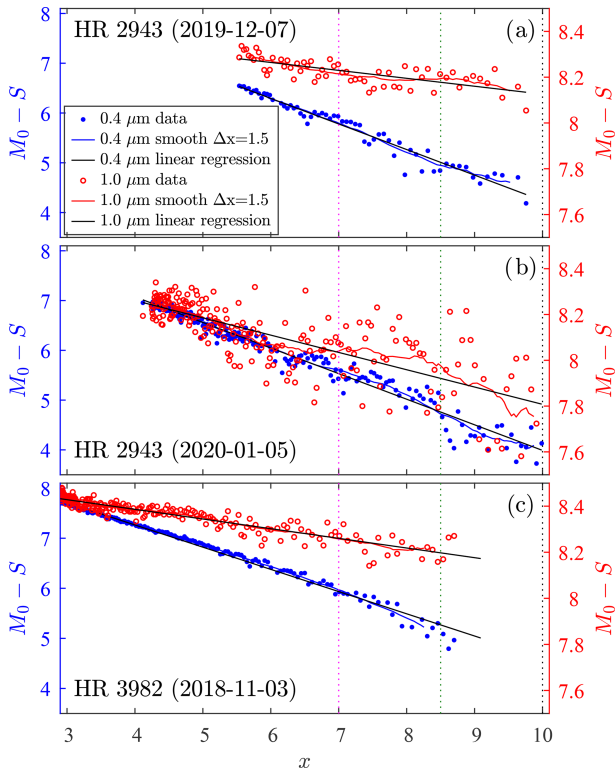
Figure 8. One-star calibrations at two spectrally distinct channels (400 and 1000 nm) for different dates and stars. The black lines represent the full regression line for all data points over the entire x range. Star measurements for the **(a)** and **(b)** cases started at the smallest x values, while the **(c)** case measurements began at the largest x value. The solid (varying) curves were generated by averaging $(M_0 - S)$ over $\Delta x = 1.5$ sliding windows. The three coloured (dotted) vertical lines correspond to the colours of the three $x_{\max}$ cases of Fig. 10.

common-signed bias (positive or negative) of the regression slope and the calibration value, relative to drift-free conditions. Figure 10a and b show spectrum-wide τ_p reduction as $x_{\max}$ and calibration time increase. This suggests spatial and/or temporal sky transparency instability during calibration. Such rapid and spectrally neutral variation is consistent with the domination of coarse-mode (super μm) particles: a (post cloud-screened) mode that is mostly dominated by spatially homogeneous cloud particles at Eureka (O'Neill et al., 2016). The near-superposition of all τ_p spectra above 500 nm in Fig. 10c indicates stable transparency that is characteristic of a cloud-free atmosphere dominated by fine-mode (submicrometre) particles. A number-density-induced drift of similar fine-mode aerosol particles will generate spectrally independent variations in $\Delta \tau_p / \tau_p$: the larger τ_p value (corresponding to the larger absolute difference in the blue/UV part of the spectrum) could explain the increasingly larger UV deviations (such as between the magenta and black/green curves in Fig. 10c).
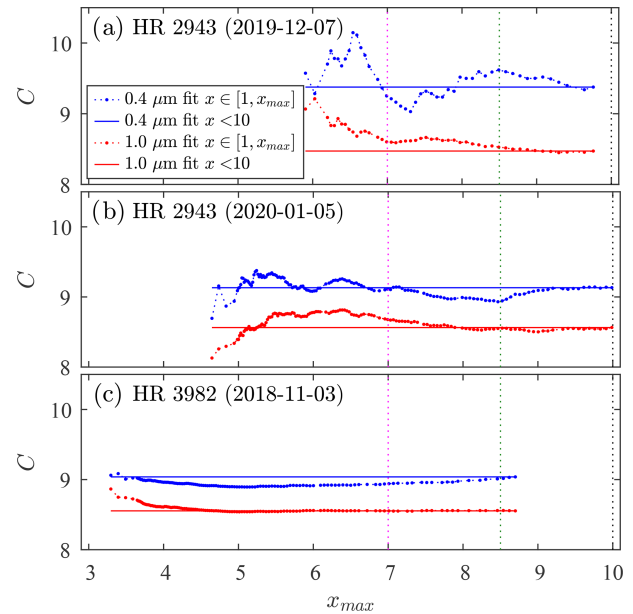
Figure 9. C values retrieved from linear regressions over an increasing x range, i.e. from the smallest x to an increasing $x_{\max}$ for all the cases plotted in Fig. 8. The horizontal reference lines represent regressions over the entire x range (the solid lines of Fig. 8), while the three coloured (dotted) vertical lines correspond to the colours of the three $x_{\max}$ cases of Fig. 10.
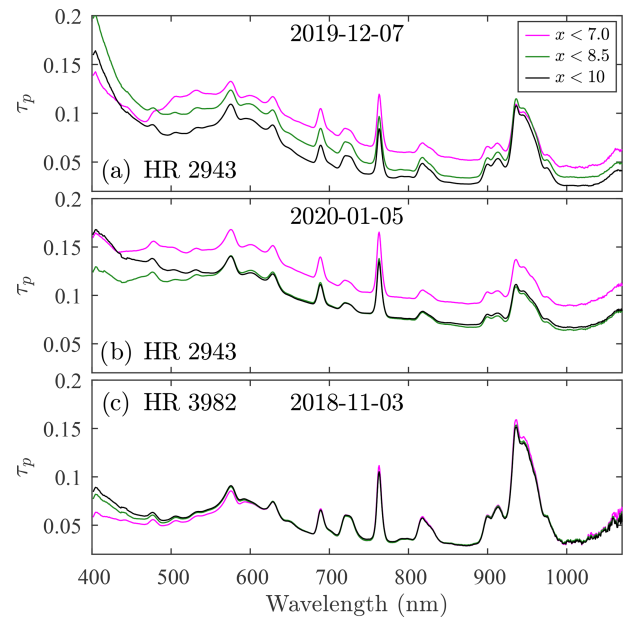
Figure 10. Optical depth (slope) spectrum retrieved from calibration performed at different x ranges.

The two bullet lists below summarize the specific processes that can lead to variations of calibration slope (τ_p) and intercept (C), traceable to real or apparent optical depth variations.

Instances of τ_p and C overestimation.

– A systematic coarse-mode τ_p increase (as described above) can have a dramatic spectrum-wide effect: flagging and discarding such measurements is, accordingly, essential. A fine-mode τ_p increase will predominantly affect the UV/blue part of the spectrum.

– Recent tests indicate that the optical collimation of the Eureka Celestron C11 telescope requires correction. Mis-collimation is responsible for a significant part of the star spot size reported in Ivănescu et al. (2021). Correcting the attendant vignetting problem (whose consequence is a decreased star flux and apparent increase in τ_p) may enable reliable measurements at x values well above the limit of $x \simeq 5$ reported by Ivănescu et al. (2021).

– The angular star spot size (ω), being proportional to $\lambda^{-1/5}x^{3/5}$ (Eqs. 4.24, 4.25 and 7.70" of Roddier, 1981), effectively leads to spectrally dependent vignetting (i.e. apparent τ_p and C increase) as a function of x: an increase in x from 7 to 9.5 would be equivalent to 20 % of ω increase for a spectral change from 400 to 1000 nm. This coupled spectral and air mass vignetting influence is consistent with Fig. C1 with the blue (0.4 μm) curve increasing at $x \simeq 7$, while the increase of the red (1.0 μm) curve occurs only at $x > 9$. This dynamic potentially dominates the large UV/blue errors seen in Figs. 7 and 10.

– Noisier star spots, attributable to increased turbulence and scintillation at large x, may induce larger centring errors and exacerbate apparent increases in τ_p and C due to vignetting.

Instances of τ_p and C underestimation.

– There is a systematic τ_p decrease during the calibration period (notably when the calibration starts at large τ_p).

– Weak signals, usually at large x and notably for hot stars in the NIR, may lead to sensitivity loss due to ADC (analog to digital conversion) limitations and attendant slope and intercept (τ_p and C) reductions.

These factors contribute to Fig. 10 τ_p dynamics and likely relate to the one-star $\sigma_{\hat{C}}$ spectra shown in Fig. 7. A very similar spectrum is indeed observed in the case of one faint star at large air mass (Fig. 11). Such spectral dynamics, possibly dominated by the aforementioned spectral influence of vignetting, are also likely related to the similar M_0 bias spectra shown in Figs. 4 and 11 of Ivănescu et al. (2021). The identification of the M_0 bias source is of paramount importance, as it may guide strategical observation choices made to improve the accuracy of future star catalogues. The error envelopes about the M_0 bias (quantified in Fig. 12) add an additional, roughly flat spectral component (in spectral regions other than those that are dominated by H-absorption bands).
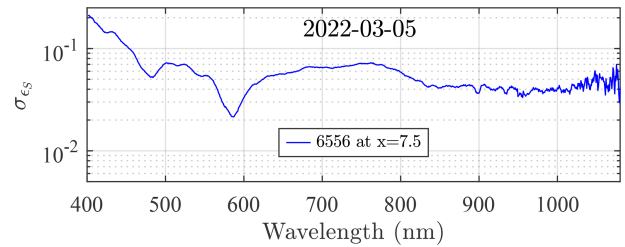
Figure 11. Standard deviation of S magnitude measurements at large air mass for a faint catalogue star (HR 6556, $V = 2.08$).
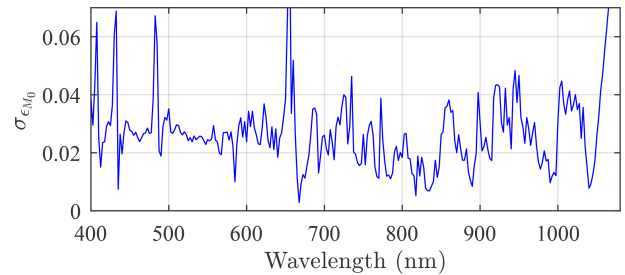
Figure 12. Standard deviation of M_0 errors deduced from the error bars of Fig. 4 in Ivănescu et al. (2021).

The smoother NIR errors in the one-star case (comparing the black one-star curve with the red multi-star curve of Fig. 5a for $\lambda > 1050$ nm) are likely due to the strong NIR signal of the much colder Procyon star. One can take advantage of this effect and develop an observing strategy that avoids using faint stars at large air mass in Eureka and still employ 12 catalogue stars at $x < 8$ in a multi-star calibration lasting 2.5 h (see Fig. A2). The star selection operation for a given multi-star calibration should also include a random air mass selection to mitigate accuracy errors attributable to systematic optical depth variations (as an alternative to the Rufener, 1986, method). Mitigation of both starlight reduction impacts at large air mass and systematic optical depth variations is a singular advantage of the multi-star vs. one-star calibration.

7 Conclusions

It was determined that no Eureka star movement satisfied an optimal sky-transit scenario of maximum possible air mass range within the constraint of $x < 5$. The solution to this intrinsic shortcoming of a High Arctic site is to perform multi-star calibrations: this approach incorporates the fundamental advantage of reducing the calibration period and thus minimizing optical depth variability. It is, by its very nature, a calibration that enables the retrieval of a star-independent calibration parameter.

Multi-star calibration repeatability errors ($\sigma_{\hat{C}}$) were systematically smaller than the single-star errors and, in the central part of the spectrum, approached the target value of 0.01 for an observing period of 2.5 h. Those errors were

partly affected by less than optimal clear-sky conditions (notably in the presence of cloud), with τ_p slightly larger than the recommended "clear-sky" value of 0.13: see Sect. 4 and Appendix A). Coarse-mode filtering algorithms, that ideally eliminate all influences of coarse-mode optical depth specifically in a calibration scenario, are necessary to ensure the best calibration[10]. Large UV and NIR errors can be reduced by avoiding faint stars at large x and by improving the current telescope collimation. The mitigation of mis-collimation problems can, in the short term, be affected by a constraint of $x < 7$. This can be achieved at Eureka by employing 12 constrained-magnitude stars over a 3 h calibration period (see Appendix A). A constraint of $\tau_p < 0.13$ may bring the calibration errors in the blue-to-red spectral range closer to the 0.01 target, with the remaining UV and NIR spectral regions being subject to the influence of M_0 errors.

In summary, the advantages of multi-star versus one-star calibration are star-independent calibration, faster coverage of larger air mass ranges, more calibration opportunities, and star selection capability for both mitigating the impact of starlight reduction with increasing air mass and systematic optical depth variations. These singular benefits were shown to override the drawbacks of specific star catalogue errors (i.e. the multi-star calibration performs better than the one-star case, even if the former is uniquely affected by M_0 errors). Further improvement will only be achieved by developing a more accurate extraterrestrial star-magnitude catalogue: their UV/blue errors, likely linked to large-x spectral vignetting or fine-mode aerosol variations, are endemic to current ground-based star catalogues. This improvement may be affected from a space-borne platform or at a high-elevation observatory (the primary goal being to reduce turbulence-induced star-spot size and optical depth variability). The use of a large aperture telescope (limiting scintillation and low-starlight measurement errors) and a larger FOV instrument (less prone to vignetting) will, in general, provide better results.

Appendix A: Calibration opportunities

Figure A1a shows the τ_p histogram for data acquired during the 2019–2020 observing season at Eureka[11]. The blue and red vertical lines respectively indicate the clear-sky cutoff values of 0.13 and 0.15 determined in Sect. 4 for the 2 h and 8 h calibrations. Operational conditions occurred 37 % of the time (i.e. those periods of time when measurements were not impeded by persistent thick clouds or the performance

of maintenance tasks). A frequency curve of clear-sky periods (a period for which all τ_p values are less than the cutoff value) is presented in Fig. A1b. Measurements acquired during 2 h and 8 h clear-sky periods represented, respectively, 35.5 % and 39 % of all measurements. These numbers, transformed into an estimation of clear-sky fraction of the total measurement time, yield values of 13 % and 14 % of the total contiguous seasonal time ($0.37 \cdot 0.355$ and $0.37 \cdot 0.39$, respectively). Since the measurement season is ~ 160 d (or ~ 5.3 months[12]) and given that there were 246 clear-sky periods of 2 h with $\tau_p < 0.13$, one may expect 46 such calibration periods per month. There were, on the other hand, 29 clear-sky periods of 8 h with $\tau_p < 0.15$ (or ~ 5.5 per month). If a calibration can be successfully completed in ~ 2 h, then there is a significantly larger probability-of-occurrence incentive for doing so.

The weakening of star signals with increasing air mass will progressively impact calibration quality. Figure A2 shows the availability of catalogue stars for a multi-star calibration over Eureka as a function of calibration period and maximum air mass. A calibration can, for example, be carried out in 2 h with only 11 stars of our 13-star dataset (Fig. 3). A 12-star calibration can be carried out only if $x < 9.5$ or if the calibration period is > 2.5 h.
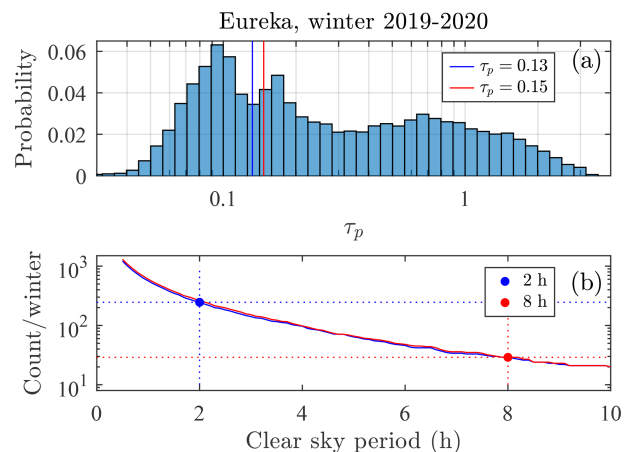

Figure A1. τ_p histogram for measurements acquired during the 2019–2020 observing season at Eureka (total of 25914 measurements). The blue and red vertical lines are the clear-sky cutoff values of 0.13 and 0.15 determined in Sect. 4. The probability is normalized so that its sum is unity **(a)**. Frequency of occurrence vs. duration of clear-sky periods **(b)**.

---

[10]Clouds are usually the dominant coarse-mode component, but coarse-mode aerosols can have diverse effects, which are typically, but not always, minor.

[11]We could speculate that the two histogram peaks near τ_p values of 0.1 and 0.16 are associated with the background fine-mode optical depth and the enhanced fine-mode optical depth incited by the presence of wind-blown sea salt (O'Neill et al., 2016).

[12]Which we pragmatically define as the number of nights for which reliable measurements can be carried out for ≥ 30 min.
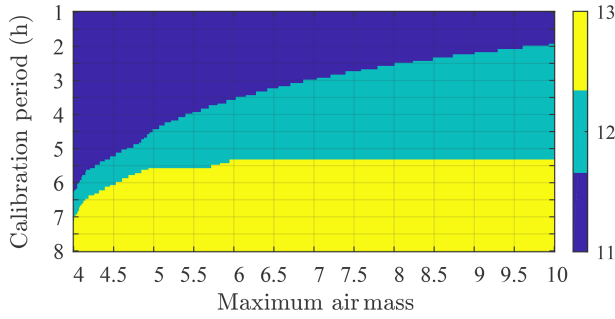
Figure A2. Number of available catalogue stars for a multi-star calibration, during a 24 h period. The following constraints were employed in generating the tri-colour contours: at least one star at $x < 1.2$ and exclusion of any star of visual magnitude $V > 1.5$ for $x > 6$, as well as $V > 2$ at $x > 5$.

Appendix B: Relative importance of component errors

From Eqs. (7) and (8) one gets the error propagation into the τ Langley retrieval:

$$\sigma_{\hat{\tau}}^2 = \frac{\sigma_{\hat{r}}^2}{\sigma_x^2} = \frac{1}{\sigma_x^2}\left(\sigma_{\bar{\epsilon}_S}^2 + \overline{x^2}\sigma_{\bar{\tau}}^2 + \sigma_{\bar{\epsilon}_{M_0}}^2\right) \quad \text{(B1)}$$

$$= k_1\sigma_{\bar{\epsilon}_S}^2 + k_2\sigma_{\bar{\tau}}^2 + k_1\sigma_{\bar{\epsilon}_{M_0}}^2, \text{ with } k_1 = \frac{1}{\sigma_x^2}, k_2 = \frac{\overline{x^2}}{\sigma_x^2}. \quad \text{(B2)}$$

Error propagation into the calibration constant (C) retrieval is, in a similar fashion, expressed as

$$\sigma_{\hat{C}}^2 = \sigma_{\hat{\tau}}^2 \overline{x^2} = \frac{\overline{x^2}}{\sigma_x^2}\left(\sigma_{\bar{\epsilon}_S}^2 + \overline{x^2}\sigma_{\bar{\tau}}^2 + \sigma_{\bar{\epsilon}_{M_0}}^2\right) \quad \text{(B3)}$$

$$= k_2\sigma_{\bar{\epsilon}_S}^2 + k_3\sigma_{\bar{\tau}}^2 + k_2\sigma_{\bar{\epsilon}_{M_0}}^2, \text{ with } k_3 = \frac{\overline{x^2}^2}{\sigma_x^2}. \quad \text{(B4)}$$

The coefficients k_1, k_2 and k_3 are displayed in Fig. B1b–d, respectively, for the x protocols of Fig. B1a. The blue curve shows uniformly distributed values of x, while the red curve shows a more realistic observing configuration of constant time intervals[13]. In order to investigate more practical (smaller) ranges, the working range is incrementally truncated from both the right and left (the solid and dashed curves, respectively). A particular focus is placed on two x ranges: the solid red circles for which $x < 5$, where $k_1 \simeq 1.2$, $k_2 \simeq 5.3$ and $k_3 \simeq 23$ (the k_3 red curve flattens out for $X > 5$ in Fig. B1d), and the open red circles for which $x > 5$, where $k_1 \simeq 0.5$, $k_2 \simeq 25$ and $k_3 \simeq 1250$ (k_3 being 50 times the "$x < 5$" value). This strong large-x weighting drives the standard error in C. $\sigma_{\epsilon_{S_z}}$ (the zenith value of σ_{ϵ_S}) is typically $\sim \sigma_\tau$, and thus $\sim \sigma_{\epsilon_{M_0}}$ (Ivănescu et al., 2021). Since ϵ_S depends on

---

[13]Both conditions apply to a star crossing the meridian at zenith.
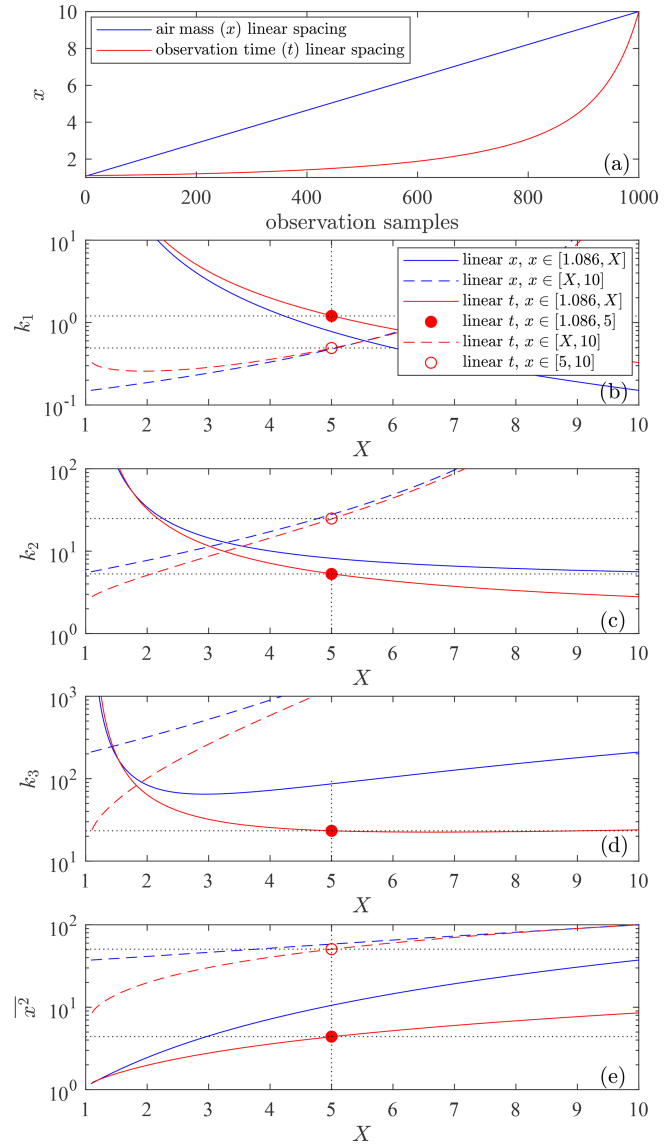
Figure B1. Variation of x as a function of the number of observation samples for measurements made in equal increments of x (blue curve) and equal increments of time (red curve) (a). The next three panels show the x-dependent variation of k_1, k_2 and k_3 (see text for more details). The legend in panel (b) applies to all the subsequent panels. Panel (e) shows $\overline{x^2}$, the $\sigma_{\hat{\tau}}^2$ to $\sigma_{\hat{C}}^2$ conversion factor of Eq. (B3).

x[14], $k_2\sigma_{\bar{\epsilon}_S}^2 \simeq k_3\sigma_{\bar{\epsilon}_{S_z}}^2$ [15]$\sim k_3\sigma_{\bar{\tau}}^2$, both first terms of Eq. (B4) being driven by k_3, which flattens out for $x \in [1.086, X]$, with $X > 5$. They will generally tend then to dominate $k_2\sigma_{\bar{\epsilon}_{M_0}}^2$

---

[14]See for example the ϵ_S increase with x in Fig. 8.
[15]If we assume $\epsilon_S \simeq \epsilon_{S_z}x$, for a multi-star calibration with $n = n_i N$ (see details in Sect. 3.2, footnote 3), $\sigma_{\bar{\epsilon}_S}^2 = \left(\sum_{i=1}^n \bar{\epsilon}_{S_i}^2\right)/n \simeq \left(\sum_{j=1}^{n_i} \epsilon_{S_z,j}^2 \sum_{k=1}^N x_k^2\right)/(n_i N) = \sigma_{\bar{\epsilon}_{S_z}}^2 \overline{x^2}$.

(unless $N \ll n$), and thus the $\sigma_{\hat{C}}$ calibration error, particularly for large x ranges.

Appendix C: Error discussion supplement

The C values, derived from tangents applied to the Fig. 8 solid curves (the means of a $\Delta x = 1.5$ sliding window), are plotted in Fig. C1. The objective of this plot is to highlight more robust (lower frequency) C variations (and thus C errors) as a function of x. The 400 nm C values are relatively stable up to $x \simeq 7$ to 7.5 where they are subject to a large increase. The 1000 nm C pattern is similar with an increase beginning at $\simeq 9$ (observations that are roughly consistent with the vignetting arguments of Sect. 6.2).
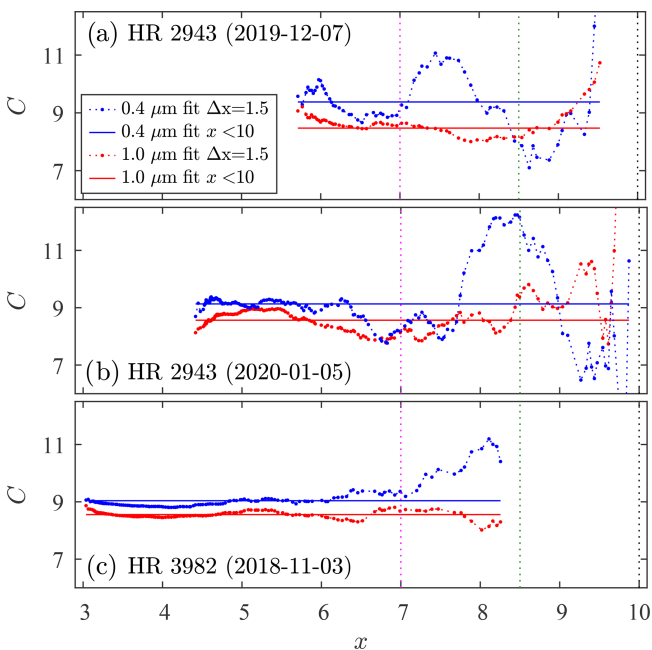
Figure C1. The variable curves show the calibration (C) variation for regressions associated with the low-frequency (sliding window) curves of Fig. 8. The horizontal lines correspond to the single C value retrieved from the full (pan-x) regression lines of Fig. 8, while the three coloured (dotted) vertical lines correspond to the colours of the three x_{max} cases of Fig. 10.

References

Alekseeva, G. A., Arkharov, A. A., Galkin, V. D., Hagen-Thorn, E., Nikanorova, I., Novikov, V. V., Novopashenny, V., Pakhomov, V., Ruban, E., and Shchegolev, D.: The Pulkovo Spectrophotometric Catalog of Bright Stars in the Range from 320 TO 1080 NM, Balt. Astron., 5, 603–838, https://doi.org/10.1515/astro-1997-0311, 1996.

Baibakov, K., O'Neill, N. T., Ivanescu, L., Duck, T. J., Perro, C., Herber, A., Schulz, K.-H., and Schrems, O.: Synchronous polar winter starphotometry and lidar measurements at a High Arctic station, Atmos. Meas. Tech., 8, 3789–3809, https://doi.org/10.5194/amt-8-3789-2015, 2015.

Barford, N.: Experimental measurements: precision, error and truth, 2nd edn., John Wiley and Sons Ltd., Chichester, https://www.worldcat.org/oclc/11622295 (last access: 4 December 2023), 1985.

Dachs, J.: Lichtelektrische Sternphotometrie und Farbenindexmessungen durch Zählung von Photoelektronen, PhD thesis, Tübingen University, https://www.worldcat.org/title/249623335 (last access: 4 December 2023), 1960.

Dachs, J.: Ein Photoelektronen zählendes Sternphotometer, Astron. Nachr., 289, 129–138, https://doi.org/10.1002/asna.19662890305, 1966.

Dachs, J., Haug, U., and Pfleiderer, J.: Atmospheric extinction measurements by photoelectric star photometry, J. Atmos. Terr. Phys., 28, 637–649, https://doi.org/10.1016/0021-9169(66)90077-8, 1966.

Goodman, L. A.: On the Exact Variance of Products, J. Am. Stat. Assoc., 55, 708–713, https://doi.org/10.1080/01621459.1960.10483369, 1960.

Gröschke, A., Herber, A. B., Schrems, O., Schulz, K.-H., and Gundermann, J.: Development and application of a new star photometer for measuring aerosol optical depth at harsh environments, in: EGU General Assembly 2009, 19–24 April 2009, Vienna, Austria, 10485, https://meetingorganizer.copernicus.org/EGU2009/EGU2009-10485.pdf (last access: 4 December 2023), 2009.

Ivănescu, L.: Une application de la photométrie stellaire à l'observation de nuages optiquement minces à Eureka, NU, Master in science thesis, UQAM, http://www.archipel.uqam.ca/id/eprint/8417 (last access: 4 December 2023), 2015.

Ivănescu, L.: Multi-star calibration in starphotometry, code and data, Zenodo [data set], https://doi.org/10.5281/zenodo.7975245, 2023.

Ivănescu, L., Baibakov, K., O'Neill, N. T., Blanchet, J.-P., and Schulz, K.-H.: Accuracy in starphotometry, Atmos. Meas. Tech., 14, 6561–6599, https://doi.org/10.5194/amt-14-6561-2021, 2021.

Montgomery, D. C. and Runger, G. C.: Applied Statistics and Probability for Engineers, 5th edn., John Wiley and Sons, Inc., http://www.worldcat.org/oclc/28632932 (last access: 4 December 2023), 2011.

Oh, Y.-L.: Retrieval of Nighttime Aerosol Optical Thickness from Star Photometry, Atmosphere, 25, 521–528, https://doi.org/10.14191/Atmos.2015.25.3.521, 2015.

O'Neill, N. T., Baibakov, K., Hesaraki, S., Ivanescu, L., Martin, R. V., Perro, C., Chaubey, J. P., Herber, A., and Duck, T. J.: Temporal and spectral cloud screening of polar winter aerosol optical depth (AOD): impact of homogeneous and inhomogeneous clouds and crystal layers on climatological-scale AODs, Atmos. Chem. Phys., 16, 12753–12765, https://doi.org/10.5194/acp-16-12753-2016, 2016.

Pérez Ramírez, D.: Caracterización del aerosol atmosférico en la ciudad de Granada mediante fotometría solar y estelar, PhD thesis, Granada, http://hdl.handle.net/10481/5628 (last access: 4 December 2023), 2010.

Pérez-Ramírez, D., Aceituno, J., Ruiz, B., Olmo, F. J., and Alados-Arboledas, L.: Development and calibration of a star photometer to measure the aerosol optical depth: Smoke observations at a high mountain site, Atmos. Environ., 42, 2733–2738, https://doi.org/10.1016/j.atmosenv.2007.06.009, 2008.

Pérez-Ramírez, D., Lyamani, H., Olmo, F. J., and Alados-Arboledas, L.: Improvements in star photometry for aerosol characterizations, J. Aerosol Sci., 42, 737–745, https://doi.org/10.1016/j.jaerosci.2011.06.010, 2011.

Pérez-Ramírez, D., Navas-Guzmán, F., Lyamani, H., Fernández-Gálvez, J., Olmo, F. J., and Alados-Arboledas, L.: Retrievals of precipitable water vapor using star photometry: Assessment with Raman lidar and link to sun photometry, J. Geophys. Res.-Atmos., 117, D05202, https://doi.org/10.1029/2011JD016450, 2012.

Roddier, F.: The Effects of Atmospheric Turbulence in Optical Astronomy, in: Progress in Optics, chap. V, Elsevier, 281–376, https://doi.org/10.1016/S0079-6638(08)70204-X, 1981.

Rousseeuw, P. J. and Croux, C.: Alternatives to the Median Absolute Deviation, J. Am. Stat. Assoc., 88, 1273–1283, https://doi.org/10.1080/01621459.1993.10476408, 1993.

Rufener, F.: Technique et réduction des mesures dans un nouveau système de photométrie stellaire, Publications de l'Observatoire de Genève, Série A: Astronomie, chronométrie, géophysique, 66, 413–464, http://www.worldcat.org/oclc/491819702 (last access: 4 December 2023), 1964.

Rufener, F.: The evolution of atmospheric extinction at La Silla, Astron. Astrophys., 165, 275–286, http://adsabs.harvard.edu/abs/1986A&A...165..275R (lsat access: 4 December 2023), 1986.

Sayer, A. M. and Knobelspiesse, K. D.: How should we aggregate data? Methods accounting for the numerical distributions, with an assessment of aerosol optical depth, Atmos. Chem. Phys., 19, 15023–15048, https://doi.org/10.5194/acp-19-15023-2019, 2019.

Soch, J., Faulkenberry, T. J., Petrykowski, K., Allefeld, C., and McInerney, C. D.: The Book of Statistical Proofs, Open, Zenodo, https://doi.org/10.5281/zenodo.5820411, 2021.

Théorêt, X.: AEROSTAR Conception d'un spectroradiomètre stellaire pour l'étude des aérosols noctures, PhD thesis, Sherbrooke, http://savoirs.usherbrooke.ca/handle/11143/2335 (last access: 4 December 2023), 2003.

Young, A. T.: Observational Technique and Data Reduction, in: Methods in Experimental Physics, vol. 12, chap. 3, Elsevier, 123–192, https://doi.org/10.1016/S0076-695X(08)60495-0, 1974.